The Astrophysical Journal Letters, 977:L18 (9pp), 2024 December 10 https://doi.org/10.3847/2041-8213/ad955f

Ultra-High-Energy Cosmic Rays Accelerated by Magnetically Dominated Turbulence

Luca Comisso[1,2,3], Glennys R. Farrar[4], and Marco S. Muzio[5,6,7]
[1] Department of Physics, Columbia University, New York, NY 10027, USA; luca.comisso@columbia.edu
[2] Department of Astronomy, Columbia University, New York, NY 10027, USA
[3] Columbia Astrophysics Laboratory, Columbia University, New York, NY 10027, USA
[4] Center for Cosmology and Particle Physics, Department of Physics, New York University, New York, NY 10003, USA; glennys.farrar@nyu.edu
[5] Department of Physics, Wisconsin IceCube Particle Astrophysics Center, University of Wisconsin, Madison, WI 53706, USA; mmuzio@icecube.wisc.edu
[6] Department of Physics, Pennsylvania State University, University Park, PA 16802, USA
[7] Department of Astronomy and Astrophysics, Pennsylvania State University, University Park, PA 16802, USA
Received 2024 September 27; revised 2024 November 20; accepted 2024 November 20; published 2024 December 4

Abstract

Ultra-high-energy cosmic rays (UHECRs), particles characterized by energies exceeding 10^{18} eV, are generally believed to be accelerated electromagnetically in high-energy astrophysical sources. One promising mechanism of UHECR acceleration is magnetized turbulence. We demonstrate from first principles, using fully kinetic particle-in-cell simulations, that magnetically dominated turbulence accelerates particles on a short timescale, producing a power-law energy distribution with a rigidity-dependent, sharply defined cutoff well approximated by the form $f_{\rm cut}(E, E_{\rm cut}) = \mathrm{sech}[(E/E_{\rm cut})^2]$. Particle escape from the turbulent accelerating region is energy dependent, with $t_{\rm esc} \propto E^{-\delta}$ and $\delta \sim 1/3$. The resulting particle flux from the accelerator follows $dN/dEdt \propto E^{-s}\,\mathrm{sech}[(E/E_{\rm cut})^2]$, with $s \sim 2.1$. We fit the Pierre Auger Observatory's spectrum and composition measurements, taking into account particle interactions between acceleration and detection, and show that the turbulence-associated energy cutoff is well supported by the data, with the best-fitting spectral index being $s = 2.1^{+0.06}_{-0.13}$. Our first-principles results indicate that particle acceleration by magnetically dominated turbulence may constitute the physical mechanism responsible for UHECR acceleration.

Unified Astronomy Thesaurus concepts: Particle astrophysics (96); High energy astrophysics (739); Cosmic rays (329); Plasma astrophysics (1261); Plasma physics (2089)

1. Introduction

The search for the sources of ultra-high-energy cosmic rays (UHECRs) is a central pursuit in astroparticle physics. While the bulk of Galactic cosmic rays are thought to be accelerated by the forward shocks of supernova remnants (A. M. Hillas 2005; P. Blasi 2013), the origin and acceleration mechanism of the highest-energy particles remain elusive and are actively debated (A. Coleman et al. 2023). Over the past decade, experimental advances have allowed the features of the all-particle energy spectrum and nuclear composition to be studied with unprecedented precision (Pierre Auger Collaboration 2020a, 2024a; Telescope Array Collaboration 2023, 2024), laying the groundwork for the development of theoretical models seeking to explain these observations.

The all-particle cosmic-ray spectrum at the highest energies reveals several distinctive features. The "ankle," observed at $\sim 5 \times 10^{18}$ eV, is marked by a pronounced hardening of the spectrum. This is followed by the "instep" at $\sim 1.3 \times 10^{19}$ eV, where the spectrum steepens. Finally, a sharp suppression is observed above $\sim 5 \times 10^{19}$ eV. The nuclear composition and its energy evolution can be inferred from the depth of maximum development of individual air showers, $X_{\rm max}$, specifically by the mean and variance of the ensemble of showers. Below the ankle, extragalactic cosmic rays are primarily protons and helium. As the energy increases, the composition becomes progressively heavier, consistent with a particle acceleration process constrained by particle rigidity, $\mathcal{R} \simeq E/eZ$. At each energy, the distribution of nuclear masses in the extragalactic component is remarkably narrow, as indicated by the small dispersion of $X_{\rm max}$ values around the mean.

Analyzing different astrophysical source scenarios and fitting the aforementioned observational data provides a means to infer the properties of the cosmic-ray spectrum at the sources (R. Aloisio et al. 2014). Inspired by theoretical predictions for shock acceleration spectra (e.g., R. J. Protheroe & T. Stanev 1999), most studies assumed that source spectra follow a power-law energy distribution with an exponential cutoff, $\phi(E) \propto E^{-s}\exp(-E/E_{\rm cut})$. With this form, fits to the data (Pierre Auger Collaboration 2017) returned spectra much harder (smaller s) than expected for the standard acceleration mechanisms, which generally predict $s \gtrsim 2$ (R. Blandford & D. Eichler 1987; M. S. Longair 2011). The hard spectral indices are required in the fits to suppress the low-energy tails of the heavier components that dominate at higher energies for consistency with the observed small variance of $X_{\rm max}$ at any given E. To address this conflict with theoretical expectations, several alternative cutoff functions, though not physically motivated, have been used in an ad hoc effort to assess the sensitivity of the best-fitting power law to the cutoff (e.g., Pierre Auger Collaboration 2017, 2023, 2024b). Among them, the broken-exponential cutoff, with a pure power law below the break energy and a pure exponential above, has become a popular choice but nonetheless yields $s \sim 1$ for the reference fits in Pierre Auger Collaboration (2017) and Pierre Auger Collaboration (2023). In some scenarios, the fits even result in negative values for s (e.g., Pierre Auger Collaboration 2017), further complicating the theoretical understanding.

In this work, we adopt a rigorous physics-based approach, leveraging large-scale fully kinetic simulations of the plasma dynamics to determine the properties of the particle energy spectrum at the source. We demonstrate that magnetically dominated turbulence accelerates ions into power-law energy spectra with spectral index around 2 and a sharp cutoff well approximated by $\phi(E) \propto E^{-s}\,\mathrm{sech}\,[(E/E_{\rm cut})^2]$. We further show that magnetically dominated turbulence accelerates particles on a very short timescale and efficiently converts a significant fraction of turbulent energy into relativistic ions. Finally, we compare the UHECR spectrum and composition at Earth from the Pierre Auger Observatory to predictions using the turbulence-based energy cutoff and predicted spectral index of escaping particles and find good agreement with the data. These results establish magnetically dominated turbulence as a compelling physical mechanism capable of resolving the challenges of UHECR acceleration.

2. Fully Kinetic Model

In the collisionless limit, the kinetic dynamics of a plasma is governed by the Vlasov–Maxwell system of equations. These equations describe the evolution of the particle distribution function $f_\alpha(\boldsymbol{x}, \boldsymbol{p}, t)$ for each particle species α at position $\boldsymbol{x}$ and momentum $\boldsymbol{p}$, together with the self-consistent electric field $\boldsymbol{E}(\boldsymbol{x}, t)$ and magnetic field $\boldsymbol{B}(\boldsymbol{x}, t)$. They evolve according to

$$\begin{aligned}
&\partial f_\alpha/\partial t = -\boldsymbol{v}\cdot\boldsymbol{\nabla} f_\alpha - q_\alpha(\boldsymbol{E}+\boldsymbol{v}\times\boldsymbol{B}/c)\cdot\partial f_\alpha/\partial\boldsymbol{p},\\
&\partial\boldsymbol{E}/\partial t = c\boldsymbol{\nabla}\times\boldsymbol{B} - 4\pi\boldsymbol{j},\\
&\partial\boldsymbol{B}/\partial t = -c\boldsymbol{\nabla}\times\boldsymbol{E},
\end{aligned} \tag{1}$$

with the constraints $\boldsymbol{\nabla}\cdot\boldsymbol{E} = 4\pi\rho$ and $\boldsymbol{\nabla}\cdot\boldsymbol{B} = 0$. The charge density $\rho(\boldsymbol{x}, t)$ and current density $\boldsymbol{j}(\boldsymbol{x}, t)$ are given by

$$\begin{aligned}
&\rho = \sum_\alpha q_\alpha \int d^3\boldsymbol{p}\, f_\alpha,\\
&\boldsymbol{j} = \sum_\alpha q_\alpha \int d^3\boldsymbol{p}\, \boldsymbol{v} f_\alpha,
\end{aligned} \tag{2}$$

where $q_\alpha = Ze$ is the species charge, e is the elementary charge, and $\boldsymbol{v}$ is the particle velocity. We solved this system along characteristics of the Vlasov equation with the particle-in-cell (PIC) method (C. K. Birdsall & B. Langdon 1985), employing the massively parallel code TRISTAN-MP (O. Buneman 1993; A. Spitkovsky 2005). The simulations do not include energy losses in the accelerator, consistent with the absence of pileup in the observed spectrum of UHECRs (R. Protheroe 2004; V. N. Zirakashvili & F. Aharonian 2007).

We performed the simulations in a triply periodic cubic domain of size L^3. The plasma consisted of electrons and ions, with combined particle density $n_{e0} + n_{i0} = n_0$. We conducted the PIC simulations with a single ion species of charge number $Z = 1$ and mass $m_i = 1836\, m_e$, i.e., protons. Computational particles were initialized according to a Maxwell–Jüttner distribution with temperature $T_{e0} = T_{i0} = T_0$, where T_{e0} and T_{i0} are the electron and ion temperatures, respectively. A uniform mean magnetic field $\boldsymbol{B}_0 = B_0\hat{\boldsymbol{e}}_z$ was imposed in the z-direction. Analogously to L. Comisso & L. Sironi (2018, 2019, 2021), we seeded turbulence by initializing a spectrum of magnetic fluctuations in a plane perpendicular to the $\boldsymbol{B}_0$ direction, given by $\delta\boldsymbol{B}(\boldsymbol{x}) = \sum_{\boldsymbol{k}} \delta B_{\boldsymbol{k}}\hat{\boldsymbol{\xi}}_{\boldsymbol{k}} \exp\,[i(\boldsymbol{k}\cdot\boldsymbol{x} + \phi_{\boldsymbol{k}})]$, where $\delta B_{\boldsymbol{k}}$ is the Fourier amplitude of the mode with wavevector $\boldsymbol{k}$, $\hat{\boldsymbol{\xi}}_{\boldsymbol{k}} = i\,\boldsymbol{k}\times\boldsymbol{B}_0/|\boldsymbol{k}\times\boldsymbol{B}_0|$ is the Alfvénic polarization unit vector, and $\phi_{\boldsymbol{k}}$ is the random phase. To ensure that $\delta\boldsymbol{B}(\boldsymbol{x})$ is a real function, we set $\delta B_{\boldsymbol{k}} = \delta B_{-\boldsymbol{k}}$ and $\phi_{\boldsymbol{k}} = -\phi_{-\boldsymbol{k}}$. We assigned equal amplitude per mode, with the summation $\sum_{\boldsymbol{k}}$ accounting for wavevector components $k_j = 2\pi n_j/L$ having mode numbers $n_j = 1, 2, 3$ in the three directions, $j = x, y, z$. These choices result in an initial outer coherence length scale for the magnetic field of approximately $l_c = L/3$.

The strength of the initial magnetic-field fluctuations is parameterized by the magnetization associated with the fluctuations, $\sigma_{\delta B} = \delta B_0^2/4\pi h_0$, where $\delta B_0 = \langle|\delta\boldsymbol{B}(\boldsymbol{x})|^2\rangle^{1/2}$ is the rms value of the fluctuations and h_0 is the enthalpy density, accounting for both ion and electron contributions. We consider strong turbulence with $\delta B_0 = B_0$. The corresponding total magnetization is $\sigma = B_{\rm rms}^2/4\pi h_0 = 2\sigma_{\delta B}$, where $B_{\rm rms} = \langle|\boldsymbol{B}(\boldsymbol{x})|^2\rangle^{1/2}$. Since we are interested in the magnetically dominated regime, we take $\sigma_{\delta B} > 1$, which yields the Alfvén speed $v_{\rm A} = c[\sigma/(1+\sigma)]^{1/2} \simeq c$. We conducted simulations with five different values of plasma magnetization, $\sigma \in \{8, 16, 32, 64, 128\}$. We also performed simulations with three different domain sizes $L/d_i \in \{250, 400, 640\}$, where $d_i = c/\omega_{pi}$ is the ion inertial length, with $\omega_{pi} = (4\pi n_0 e^2/\gamma_{0,i} m_i)^{1/2}$ indicating the ion plasma frequency and $\gamma_{0,i}$ being the mean ion Lorentz factor. We initialize the ion temperature to $k_{\rm B}T_0 = 0.2 m_i c^2$, yielding $\gamma_{0,i} \simeq 1.36$. This parameter choice does not impact our findings (L. Comisso & L. Sironi 2019). We adopt uniform grid cells of size $\Delta x = \Delta y = \Delta z = d_{e0}/2$, where $d_e = c/\omega_{pe}$ is the initial electron inertial length, with $\omega_{pe} = (4\pi n_0 e^2/\gamma_{0,e} m_e)^{1/2}$ indicating the electron plasma frequency. We use an average of 20 computational particles per cell, which adequately resolves the nonthermal particle acceleration process, as shown in L. Comisso & L. Sironi (2018, 2019). The time step is chosen according to the Courant–Friedrichs–Lewy condition, and all simulations are run for $t \geqslant 15 l_c/c$ to ensure that the particle energy spectrum has reached a steady state. We take the simulation with $\sigma = 16$ and $L/d_i = 400$ as the reference simulation.

In our simulations, turbulence develops from the initialized magnetic fluctuations and then decays in time as no continuous driving is imposed. A well-developed turbulent cascade is established on the outer-scale nonlinear timescale l_c/c. In Figures 1(a) and (b), we show a volume rendering of the vortical fields $|\boldsymbol{\nabla}\times\boldsymbol{B}|$ and $|\boldsymbol{\nabla}\times\Gamma\boldsymbol{V}|$, taken at time $t = 2.5 l_c/c$ from the reference simulation. Here, $\Gamma = [1 - (V/c)^2]^{-1/2}$ is the plasma fluid Lorentz factor, and $\boldsymbol{V}$ is the plasma fluid velocity obtained by averaging the velocities of individual particles. Sheetlike structures are ubiquitous in the turbulent domain for both fields. Due to the presence of the mean field $\boldsymbol{B}_0 = B_0\hat{\boldsymbol{e}}_z$, these structures are mostly elongated along $\hat{\boldsymbol{e}}_z$. Our large-scale PIC simulations capture the turbulent cascade from MHD scales to kinetic scales. In Figure 1(c), we present the one-dimensional spectra $P_X(k_\perp)dk_\perp = \sum_{\boldsymbol{k}\in dk_\perp} \boldsymbol{X}_{\boldsymbol{k}}\cdot\boldsymbol{X}_{\boldsymbol{k}}^*$ for the magnetic-field fluctuations ($\boldsymbol{X} = \delta\boldsymbol{B}$) and the fluid four-velocity fluctuations ($\boldsymbol{X} = \Gamma\boldsymbol{V}$). Here $k_\perp = (k_x^2 + k_y^2)^{1/2}$ represents wavenumbers perpendicular to $\boldsymbol{B}_0$. The turbulent cascade exhibits an extended MHD range, with $P_{B,\Gamma V}(k_\perp) \propto k_\perp^{-5/3}$ for $k_\perp d_i \lesssim 1$, consistent with turbulence scaling theories (P. Goldreich & S. Sridhar 1995; C. Thompson & O. Blaes 1998). At scales smaller than d_i, both spectra steepen as the turbulent cascade progresses into the kinetic range (e.g., C. H. K. Chen et al. 2014).

3. Nonthermal Particle Acceleration

Previous large-scale PIC simulations have demonstrated that large-amplitude turbulence ($\delta B_0 \sim B_0$) in a highly magnetized

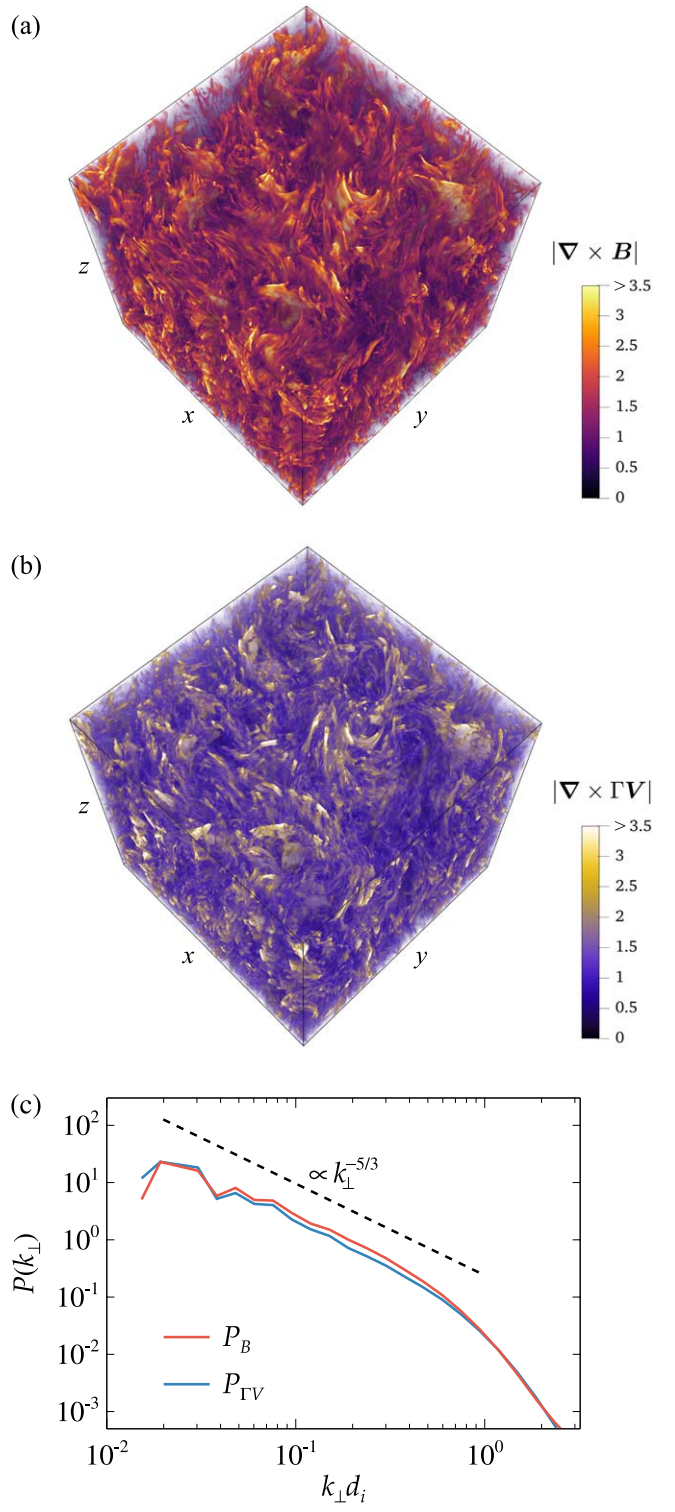

Figure 1. Volume rendering of (a) $|\nabla \times \boldsymbol{B}|$ and (b) $|\nabla \times \Gamma \boldsymbol{V}|$ (normalized to their respective rms values) taken at $t = 2.5 l_c/c$ from the reference turbulence simulation ($\sigma = 16$, $l_c/d_i = 133$). (c) One-dimensional spectra of the turbulent magnetic field (red) and fluid four-velocity (blue) at $t = 2.5 l_c/c$. Each spectrum is normalized so that $\sum_{k_\perp} P(k_\perp) = 1$. A power-law slope of $k_\perp^{-5/3}$ (dashed black line) is shown for reference.

plasma ($\sigma \gg 1$) produces a significant population of nonthermal particles with a power-law energy distribution that is independent of microscopic kinetic scales (L. Comisso & L. Sironi 2018, 2019; for results on moderately magnetized

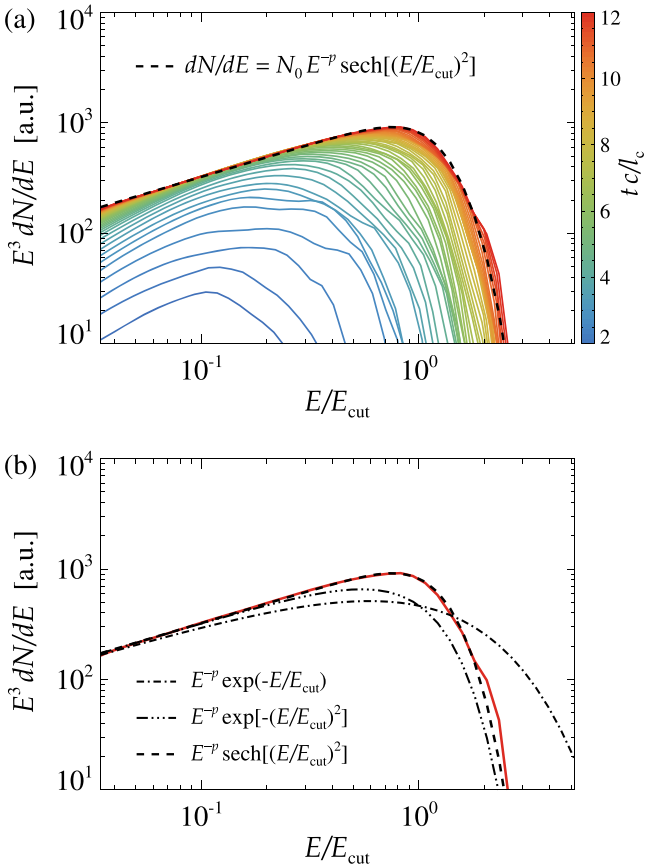

Figure 2. (a) Time evolution of the ion energy spectrum dN/dE, multiplied by E^3, for the reference turbulence simulation ($\sigma = 16$, $l_c/d_i = 133$). At late times, when the particle energy spectrum ceases to evolve, it exhibits a power-law distribution with a sharp cutoff. The spectrum is well fitted by the function $N_0 E^{-p}\,\mathrm{sech}[(E/E_{\rm cut})^2]$, where $p = 2.4$, N_0 is a normalization factor, and $E_{\rm cut}$ is the cutoff energy given by Equation (3), with $\kappa = 0.65$. (b) $E^3 dN/dE$ at saturation, with $t = 12 l_c/c$ (solid red line), overlaid with the functional forms $E^{-p}\exp(-E/E_{\rm cut})$ (dotted–dashed black line), $E^{-p}\exp[-(E/E_{\rm cut})^2]$ (triple dotted–dashed black line), and $E^{-p}\,\mathrm{sech}[(E/E_{\rm cut})^2]$ (dashed black line).

turbulence, see V. Zhdankin et al. 2018). Here, we focus on the particle energy cutoff to determine whether magnetized turbulence can serve as the mechanism responsible for UHECR acceleration, as the functional shape of the energy cutoff is closely tied to the UHECR spectrum and composition observables.

Particle acceleration via magnetized turbulence is affected by the particle's magnetic rigidity $\mathcal{R} = |\boldsymbol{p}|c/q$, as the interaction with turbulence fluctuations depends on the Larmor radius $\rho_L \simeq |\boldsymbol{p}|c/qB$ (taking $|\boldsymbol{p}| \simeq p_\perp$). Particles are effectively accelerated until their Larmor radius becomes comparable to the coherence length of the magnetic field, i.e., $\rho_L(\mathcal{R}_{\rm cut}) = \kappa l_c$, with $\kappa = \mathcal{O}(1)$. For ultrarelativistic particles, this translates to a cutoff energy estimate:

$$E_{\rm cut} = Ze\mathcal{R}_{\rm cut} = Ze\, B_{\rm rms}\, \kappa\, l_c. \tag{3}$$

In the following, we show that $\kappa = \mathcal{O}(1)$ and that the particle energy spectrum is characterized by a very sharp cutoff at this energy.

In Figure 2(a), we show the time evolution of the ion energy spectrum dN/dE, multiplied by E^3, for the reference turbulence simulation. At late times, when the turbulent energy has predominantly transferred to the particles, the spectrum ceases evolving (orange and red lines) and can be described by a

relation of the form

$$\frac{dN}{dE} = N_0 E^{-p} f_{\rm cut}(E, E_{\rm cut}), \tag{4}$$

with a cutoff that closely follows

$$f_{\rm cut}(E, E_{\rm cut}) = \mathrm{sech}\left[\left(\frac{E}{E_{\rm cut}}\right)^2\right], \tag{5}$$

with $\kappa = 0.65$ in the fit. In Figure 2(b), we compare the fit provided by the cutoff given by Equation (5) with the simple exponential cutoff $f_{\rm cut} = \exp(-E/E_{\rm cut})$. We also show $f_{\rm cut} = \exp[-(E/E_{\rm cut})^2]$, which approximates the behavior of Equation (5) for $E \gg E_{\rm cut}$. Both functions exhibit smoother behavior compared to the actual cutoff observed in the simulation, with the exponential cutoff $\exp(-E/E_{\rm cut})$ significantly failing to represent the PIC simulation results.

In Figure 3, we compare the late-time particle energy spectra from simulations with varying magnetization σ (panel (a)) and different turbulence inertial ranges l_c/d_i (panel (b)). In these simulations, σ is varied by changing the magnetic-field strength ($\sigma \propto B_{\rm rms}^2$), while l_c/d_i is varied by changing l_c. Figures 3(a) and (b) show that all simulations produce the same sharp cutoff. When the cutoff energy $E_{\rm cut}$ is accounted for using Equation (3), the cutoffs align at the same characteristic energy, where $\kappa = 0.65$ has been used for all cases. It is also noteworthy that, as the total particle count increases (i.e., as l_c/d_i increases), the slight excess of particles at $E/E_{\rm cut} \gtrsim 2$ diminishes, indicating that this excess is an artifact of limited particle statistics.

In all simulations, we measured the fraction of dissipated magnetic energy that is converted into ion energy at the time when the ion energy spectrum reaches a steady state. This is reported in Figure 3(c). Across variations in magnetization σ and inertial range l_c/d_i, approximately 50% of the dissipated magnetic energy is consistently converted into ions, in line with earlier simulations of nonrelativistic turbulence with $\delta B_0 \sim B_0$ (L. Comisso & L. Sironi 2022).

To characterize particle dynamics, we tracked the time evolution of $\sim 3 \times 10^7$ particles (protons) that were randomly selected from our reference simulation. For these particles, we computed the work done by the parallel and perpendicular electric fields, $W_{\parallel,\perp}(t) = q\int_0^t \boldsymbol{E}_{\parallel,\perp}(t') \cdot \boldsymbol{v}(t')\, dt'$, where the parallel ($\parallel$) and perpendicular ($\perp$) components are defined with respect to the local magnetic field, i.e., $\boldsymbol{E}_\parallel = (\boldsymbol{E}\cdot\boldsymbol{B})\boldsymbol{B}/B^2$ and $\boldsymbol{E}_\perp = \boldsymbol{E} - \boldsymbol{E}_\parallel$. This enables us to isolate the relative contributions of the accelerating electric field components by constructing the distribution $f(W_{\rm tot},\ W_\perp/W_{\rm tot})$, where $W_{\rm tot} = W_\parallel + W_\perp$. This distribution, normalized such that $\int_0^1 f(W_{\rm tot}, W_\perp/W_{\rm tot})\, d(W_\perp/W_{\rm tot}) = 1$, is shown in Figure 4(a). When $W_{\rm tot} \lesssim \sigma E_0$, where E_0 is the initial particle energy, most of the particle energization occurs via $\boldsymbol{v}\cdot\boldsymbol{E}_\parallel$. This energization stage is associated with the nonideal MHD reconnection electric field, as discussed in L. Comisso & L. Sironi (2018, 2019). After this initial phase, particles gain energy via $\boldsymbol{v}\cdot\boldsymbol{E}_\perp$ by interacting with large-scale turbulent fluctuations. For particles well into the MHD inertial range of the turbulence cascade, the motional electric field $\boldsymbol{E}_\perp \simeq -(\boldsymbol{V}/c)\times\boldsymbol{B}$ becomes the dominant acceleration channel, with $W_\perp \gg W_\parallel$ for $W_{\rm tot} \gg \sigma E_0$.

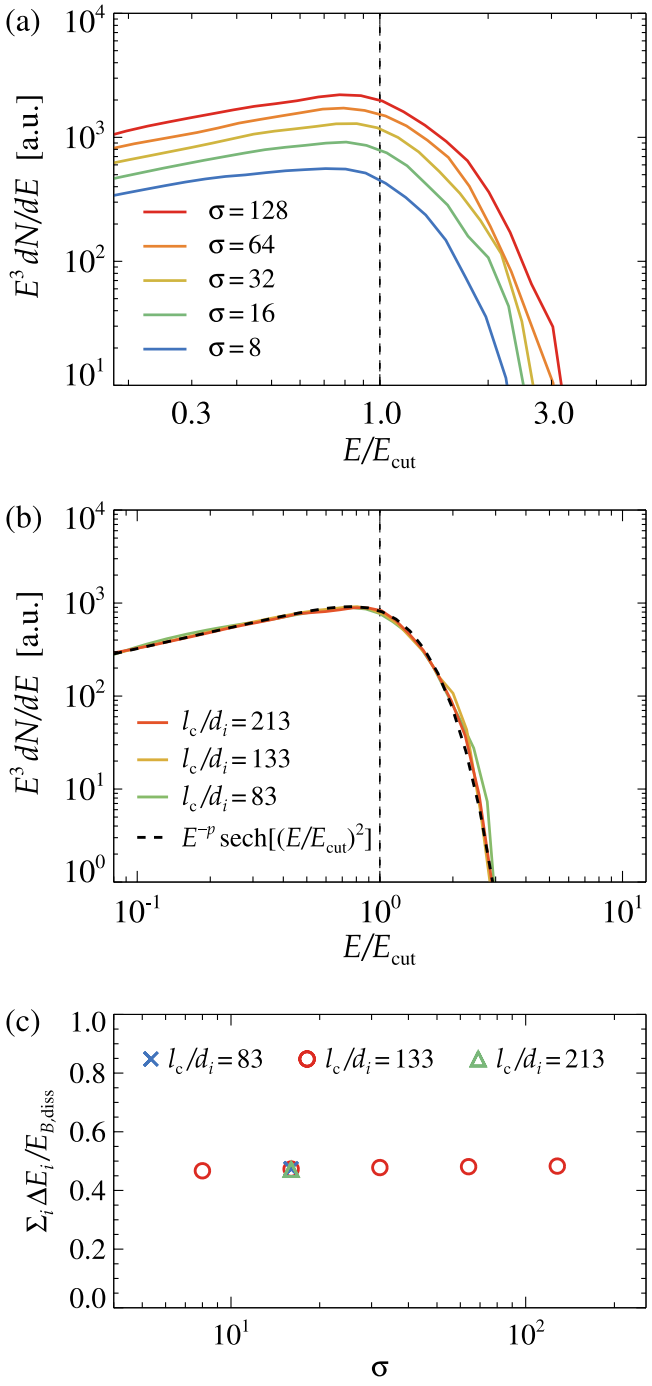

Figure 3. (a) Ion energy spectra at saturation ($t = 12 l_c/c$) for turbulence simulations with varying magnetization $\sigma =$ (8, 16, 32, 64, 128) and fixed $l_c/d_i = 133$. In all cases, the particle energy spectrum exhibits a cutoff at $E_{\rm cut}$ as given by Equation (3). (b) $E^3 dN/dE$ for simulations with varying $l_c/d_i =$ (83, 133, 213) and fixed $\sigma = 16$, overlaid with $dN/dE \propto E^{-p}\,\mathrm{sech}[(E/E_{\rm cut})^2]$, where $p = 2.4$ (dashed black line). (c) Fraction of dissipated magnetic energy, $E_{B,\rm diss}$, converted to ion energy at $t = 12 l_c/c$ across the different simulations in our study.

Acceleration via stochastic interactions with turbulent fluctuations can be characterized by an effective diffusion coefficient in energy space for particles whose gyroradii fall within the turbulence inertial range, $d_i < \rho_L < l_c$. Using the trajectories of particles in the simulation (i.e., not test particles) we compute the mean square energy variation $\langle(\Delta E)^2\rangle$ for particles that have energy E at time t_*, based on their energy in

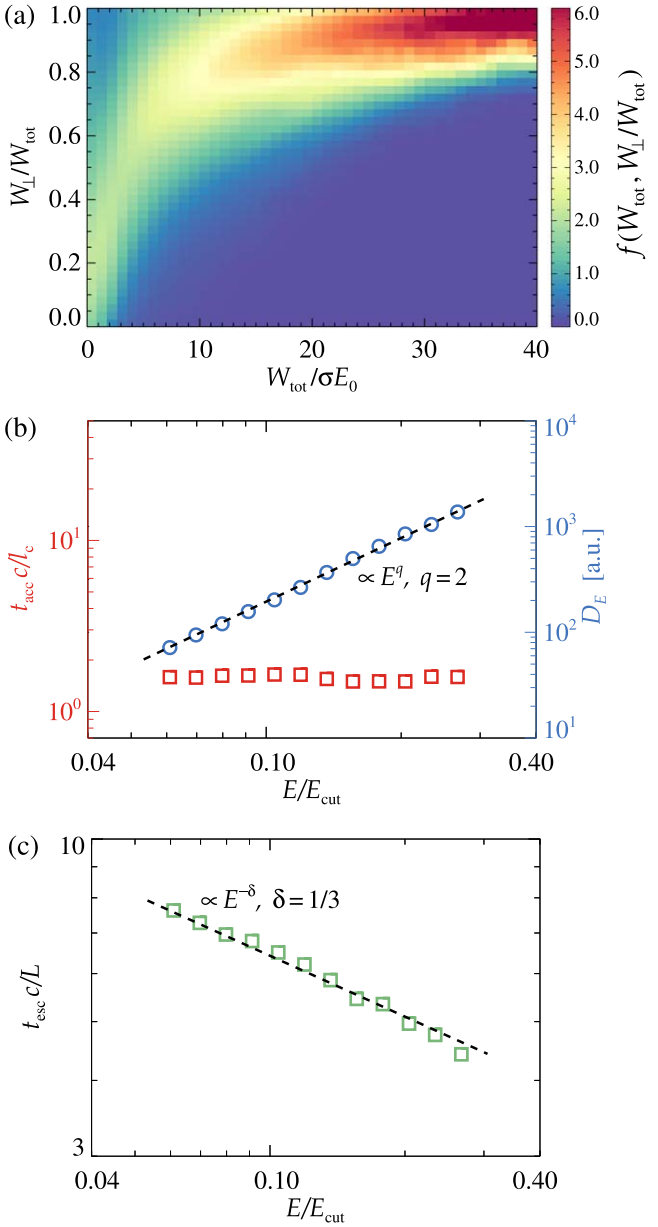

Figure 4. (a) Particle distribution in terms of $W_{\rm tot}$ and $W_\perp/W_{\rm tot}$ obtained from tracked particles in the reference turbulence simulation ($\sigma = 16$, $l_c/d_i = 133$). (b) Energy diffusion coefficient D_E (blue circles) and stochastic acceleration timescale $t_{\rm acc} = E^2/4D_E$ (red squares), evaluated at $ct_*/l_c = 3$ with a time interval $c\Delta t/l_c = 1.75$. A reference power law $D_E \propto E^q$ with a slope of $q = 2$ is also shown. (c) Escape timescale $t_{\rm esc}$ as a function of particle energy (green squares), evaluated starting at $ct_*/l_c = 3$. A power law $t_{\rm esc} \propto E^{-\delta}$ with slope $\delta = 1/3$ is provided for reference.

the frame comoving with the drift velocity $c\boldsymbol{E}\times\boldsymbol{B}/B^2$. The effective diffusion coefficient is then given by $D_E = \langle(\Delta E)^2\rangle/2\Delta t$, where $\Delta t = t - t_*$. Δt must be sufficiently long that the initial conditions have negligible impact and short enough that the turbulence properties have not significantly changed over this interval. For this purpose, we adopt a time interval $c\Delta t/l_c = 1.75$, starting from $ct_*/l_c = 3$. The resulting energy diffusion coefficient as a function of particle energy is shown in Figure 4(b) with blue circle symbols. We find $D_E \propto E^2$, similarly to what has been found in PIC simulations of electron–positron plasmas (L. Comisso & L. Sironi 2019; K. Wong et al. 2020) and test-particle simulations in MHD turbulence (J. W. Lynn et al. 2014; S. S. Kimura et al. 2019; X. Sun & X.-N. Bai 2021; O. Pezzi et al. 2022). Given D_E, the stochastic acceleration timescale can be estimated as

$$t_{\rm acc} = \frac{E^2}{4D_E}, \tag{6}$$

which is shown in Figure 4(b) with red square symbols. For the stochastic particle acceleration process relevant here, the acceleration timescale can be expressed as (e.g., L. Comisso & L. Sironi 2019; M. Lemoine 2019)

$$t_{\rm acc} \simeq \frac{1}{4\kappa_{\rm acc}\delta u^2}\frac{B^2_{\rm rms}}{\delta B^2_{\rm rms}}\frac{l_c}{c}, \tag{7}$$

where $\delta u^2 = \Gamma^2\beta_V^2$ is the squared four-velocity of the scatterers and $\kappa_{\rm acc} \simeq 0.1$ from PIC simulations (L. Comisso & L. Sironi 2019). This stochastic acceleration timescale differs from the commonly assumed, slower, energy-dependent gyroresonant acceleration adopted under the assumption of quasi-linear theory (e.g., R. Schlickeiser & J. A. Miller 1998; H. Yan & A. Lazarian 2002; G. Brunetti & A. Lazarian 2011; S. Kundu et al. 2023). For large-amplitude turbulence, this stochastic acceleration timescale is comparable to the outer-scale eddy turnover time.

We next examine the energy dependence of particle escape from the accelerator. The effective scattering mean-free path, λ_s, scales with the Larmor radius as $\lambda_s \simeq l_c(\rho_L/l_c)^\delta$, with $\delta > 0$, namely, longer residence times for lower-energy particles. The residence time within the accelerator can then be expressed as

$$t_{\rm esc} \simeq \frac{L^2}{\lambda_s c} \simeq \frac{L^2}{l_c c}\left(\frac{E_{\rm cut}}{E}\right)^\delta \propto E^{-\delta} \tag{8}$$

for ultrarelativistic particles. Here, we evaluate this energy dependence directly from the self-consistent trajectories of the tracked particles. For particles binned by energy as in the evaluation of D_E, we record the time Δt_{l_c} it takes for them to move perpendicular to $\boldsymbol{B}_0$ from their initial coordinates (x_*, y_*) at time t_* and travel a distance greater than l_c, i.e., $[(x - x_*)^2 + (y - y_*)^2]^{1/2} > l_c$. We consider only particles that remain within the same energy bin and compute the average $\langle\Delta t_{l_c}\rangle$ for each energy bin. The escape time from the accelerator is then given by $t_{\rm esc}(E) \propto \langle\Delta t_{l_c}\rangle(E)$. The resulting escape timescale as a function of particle energy is shown in Figure 4(c) with green square symbols. Our findings indicate that $t_{\rm esc} \propto E^{-1/3}$ offers a reasonable approximation of the PIC simulation results. This scaling is broadly consistent with test-particle simulations (e.g., F. Casse et al. 2001; P. Kempski et al. 2023; M. Lemoine 2023), which commonly report δ values in the range $0.3 \leqslant \delta \leqslant 0.5$.

The energy-dependent escape timescale results in a hardened escaping-particle energy spectrum compared to the spectrum within the accelerator. Accounting for the escape timescale, the flux of particles escaping the accelerator is given by

$$\phi(E) = \frac{dN}{dEdt} = \frac{1}{t_{\rm esc}}\frac{dN}{dE} \propto E^{-s}\,{\rm sech}\left[\left(\frac{E}{E_{\rm cut}}\right)^2\right], \tag{9}$$

where $s = p - \delta$. The spectral index s characterizes the particles "injected" by the accelerator into the surrounding environment. From our turbulence simulations, displaying typical values of

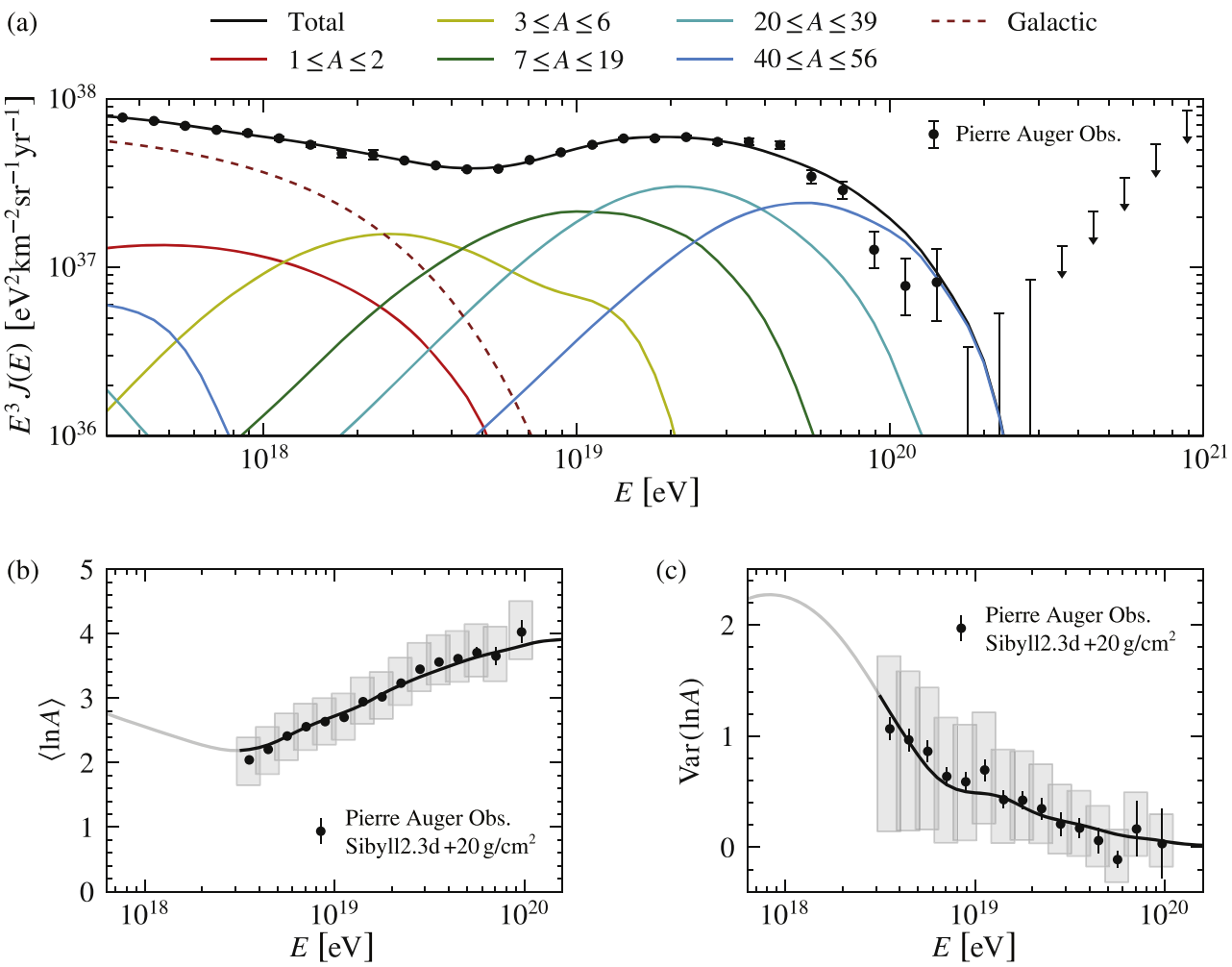

Figure 5. Cosmic-ray energy spectrum (top panel) and the first two moments of the $\ln A$ distribution (bottom panels) at Earth based on the turbulence acceleration model. In this model, the individual element spectra at the source are given by $\phi_A(E) = f_A\,\phi_{\rm ref}(E/E_{\rm ref})^{-s}\,{\rm sech}[(E/Ze\mathcal{R}_{\rm cut})^2]$. The best fit to the data is given by the spectral index $s = 2.1^{+0.06}_{-0.13}$ and the cutoff rigidity $\log_{10}(\mathcal{R}_{\rm cut}/{\rm V}) = 18.8^{+0.02}_{-0.02}$. Data points are the Pierre Auger Observatory's 2021 spectrum (P. Abreu et al. 2021) and composition based on surface detector data (Pierre Auger Collaboration 2024c). Error bars denote the statistical uncertainties (1σ statistical errors), and the shaded boxes illustrate the experimental systematic uncertainties (1σ systematic errors) of the composition. The composition data are interpreted via the hadronic interaction model SIBYLL2.3D (F. Riehn et al. 2020).

$p \sim 2.4$ and $\delta \sim 1/3$, we obtain a characteristic spectral index of $s \sim 2.1$.

4. UHECR Spectrum and Composition

Using the form of the source particle energy spectra given by the turbulence acceleration model, Equation (9) with Equation (3), and the code developed in M. Unger et al. (2015) and M. S. Muzio & G. R. Farrar (2023), we calculate the propagation of the UHECRs starting from their injection into the environment surrounding the accelerator, including their interactions in that region, and continuing with their interactions with the cosmic microwave background (CMB) and the extragalactic background light (EBL) prior to detection. We explore the multidimensional parameter space of injected spectral index, cutoff rigidity, and initial composition, as well as key properties of the environment such as peak energy of the photon field and ratio of escape and interaction time, comparing the predicted spectrum and composition observables to the spectrum and nuclear composition observed at Earth. The treatment takes into account the following interactions with the ambient photon field: (i) pion photoproduction $p + \gamma \to \pi + p$ (which, for interactions with CMB photons, leads to the so-called Greisen–Zatsepin–Kuzmin cutoff; K. Greisen 1966; G. T. Zatsepin & V. A. Kuz'min 1966), (ii) photodisintegration of nuclei in both the source environment and during extragalactic propagation via interactions with CMB and EBL photons, $A + \gamma \to (A - nN) + nN$, where n is the number of nucleons lost by the nucleus, and (iii) pair photoproduction $p + \gamma \to e^+ + e^- + p$ (Bethe–Heitler process) during extragalactic propagation. Extragalactic propagation was simulated using CRPROPA3 (R. Alves Batista et al. 2016), adopting the EBL model of R. C. Gilmore et al. (2012) and a star formation rate source evolution (B. E. Robertson et al. 2015).

A combination of different injection elements is used as an approximation of different mass groups in the cosmic-ray composition. Each of these elements is characterized by the same power-law index s, and their spectra are given by $\phi_A(E) = f_A\,\phi_{\rm ref}(E/E_{\rm ref})^{-s}\,{\rm sech}[(E/E_{\rm cut})^2]$, where $E_{\rm ref} = 10^{17}$ eV is a reference energy selected below the minimum cutoff energy for protons, $\phi_{\rm ref}$ is a normalization constant, and the injection fraction f_A, which is defined as the relative number flux ratios at the same reference energy $E_{\rm ref}$, is determined through the fit. We approximate the Galactic cosmic-ray component as a single $A = 38$

composition, with the spectral index and composition treated as auxiliary parameters. For details, see M. Unger et al. (2015), M. S. Muzio et al. (2022), and M. S. Muzio & G. R. Farrar (2023).

We fit the model predictions to the UHECR spectrum and composition data of the Pierre Auger Observatory (Pierre Auger Collaboration 2020a, 2020b; P. Abreu et al. 2021; Pierre Auger Collaboration 2024c) as detailed in M. S. Muzio & G. R. Farrar (2023). We map $\langle X_{\rm max}\rangle$ and $\mathrm{Var}(X_{\rm max})$ data into $\langle \ln A\rangle$ and $\mathrm{Var}(\ln A)$ using the parameterization of the Pierre Auger Collaboration (2013), after shifting the $\langle X_{\rm max}\rangle$ predictions of the hadronic interaction model SIBYLL2.3D (F. Riehn et al. 2020) by $+20\,\mathrm{g\,cm^{-2}}$ following the Pierre Auger Collaboration (2024d). To assess the goodness of fit, we compute a combined χ^2 to the spectrum data and composition:

$$\chi^2 = \sum_i^{N_{\rm spec}} \frac{(J_{m,i}-J_i)^2}{\sigma^2_{J,i}} + \sum_j^{N_{\rm comp}} \frac{(\langle \ln A\rangle_{m,j}-\langle \ln A\rangle_j)^2}{\sigma^2_{\langle \ln A\rangle,j}} + \sum_j^{N_{\rm comp}} \frac{(\mathrm{Var}(\ln A)_{m,j}-\mathrm{Var}(\ln A)_j)^2}{\sigma^2_{\mathrm{Var}(\ln A),j}}, \quad (10)$$

where $N_{\rm spec}$ and $N_{\rm comp}$ are the number of data points in the spectrum and composition, respectively; $\mathcal{Q}_{m,i}$ denotes the model prediction for the quantity $\mathcal{Q}$ (differential flux J, mean logarithmic mass number $\langle \ln A\rangle$, or its variance $\mathrm{Var}(\ln A)$) at energy bin i; and errors include only statistical errors for the energy spectrum from the Pierre Auger Collaboration (2020a, 2020b), P. Abreu et al. (2021), and the mean and variance of $\ln A$ from the Pierre Auger Collaboration (2024c). For spectral energy bins above the highest-energy data point, we follow S. Baker & R. D. Cousins (1984) by adding an additional $2n_i$ to the χ^2, where n_i is the expected number of observed events predicted by the model in energy bin i given the exposure of the data set. Our final figure of merit is $\chi^2_{\rm tot} = \chi^2 + 2\sum_i n_i$, where i runs over energy bins above the highest-energy data point in the spectrum.

Figure 5 shows the predicted energy spectrum $J(E) = dN/dEdtdAd\Omega$, multiplied by E^3, along with the composition moments $\langle \ln A\rangle$ and $\mathrm{Var}(\ln A)$, based on the best-fit model parameters. We explored source spectral indices within the range $1 < s < 3$, motivated by standard electromagnetic acceleration mechanisms. The turbulence-based model results in a best-fit source spectral index of $s = 2.1^{+0.06}_{-0.13}$, based on the χ^2 goodness-of-fit test (see Figure 6), with a cutoff rigidity $\log_{10}(\mathcal{R}_{\rm cut}/\mathrm{V}) = 18.8^{+0.02}_{-0.02}$. We note that the exact best-fit value of the spectral index and its uncertainty are sensitive to the composition data set used for the fitting but are qualitatively unchanged.

As could be expected, the turbulence-based $\mathrm{sech}[(E/E_{\rm cut})^2]$ cutoff compresses the energy range over which each element group significantly contributes, as required for consistency with the narrowness of the $\ln A$ distribution. This results in a relatively soft power-law index at the source ($s \sim 2$–2.2) that is consistent with our PIC simulation results. By contrast, the same analysis but using the exponential cutoff gives a worse fit and requires a spectral index $s = 1.26^{+0.1}_{-0.1}$, incompatible with diffusive shock acceleration theory. It is worth noting that in both cases, the power-law spectrum leaving the source environment is roughly one unit harder than that given by the accelerator, due to lower-rigidity particles undergoing more interactions before escaping the source environment (M. Unger et al. 2015).

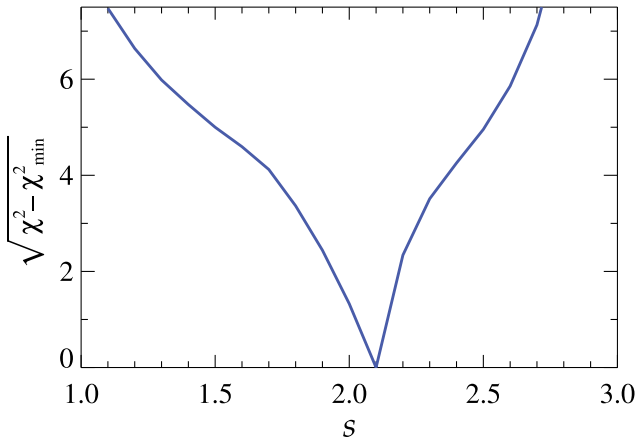

Figure 6. $\sqrt{\chi^2-\chi^2_{\rm min}}$ as a function of the source spectral index s for the turbulence acceleration model, where the individual element spectra from the accelerator are given by Equation (9) with $E_{\rm cut} = Ze\mathcal{R}_{\rm cut}$.

For the best-fit results shown in Figure 5, taking into account all element groups, we obtain that the volumetric energy-injection rate of UHECRs, $\mathcal{L}_{\rm UHECR}$, defined as the total energy injected per unit of comoving volume per unit time at redshift $z = 0$, is

$$\mathcal{L}_{\rm UHECR} = \sum_A \int_{E_a}^{E_b} EQ_A(E)dE \simeq 0.7 \times 10^{45}\,\mathrm{erg\,Mpc^{-3}yr^{-1}}, \quad (11)$$

where $Q_A(E)$ indicates the number of nuclei with atomic mass number A injected per unit of energy, volume, and time, and the integration limits are $E_a = 10^{18}$ eV and $E_b = 10^{21}$ eV. This volumetric energy-injection rate, which is about a factor of 2 larger than found with the exponential cutoff with its associated required harder spectral index, is compatible with different source classes, including jets from active galactic nuclei (AGNs), gamma-ray bursts, and tidal disruption events, where magnetized turbulence is expected to be at play.

5. Conclusions

We have demonstrated, using fully kinetic PIC simulations, that particle acceleration by magnetically dominated turbulence possesses the properties needed to explain the acceleration of UHECRs. After a low-energy injection phase driven by magnetic-field-aligned electric fields, ions are accelerated by scattering off turbulent fluctuations, gaining energy through the motional electric field, up to the cutoff energy $E_{\rm cut} = Ze\mathcal{R}_{\rm cut} = ZeB_{\rm rms}\kappa l_c$, with $\kappa \simeq 0.65$. This acceleration process occurs on a short, energy-independent timescale, which, for large-amplitude turbulence, is comparable to the outer-scale eddy turnover time. The resulting particle energy spectrum follows a power law with a sharp cutoff at the characteristic energy scale $E_{\rm cut}$. Taking into account the energy dependence of particle escape from the accelerator, the spectrum of relativistic ions produced by magnetically dominated turbulence at the source is well approximated by $dN/dEdt \propto E^{-s}\,\mathrm{sech}[(E/E_{\rm cut})^2]$ with $s \sim 2.1$. The $\mathrm{sech}[(E/E_{\rm cut})^2]$ cutoff is considerably sharper than the $\exp(-E/E_{\rm cut})$ cutoff expected for diffusive shock acceleration, enabling softer particle spectra

at the source to explain the UHECR spectrum and composition observed at Earth.

We have fit the Pierre Auger Observatory's spectrum and composition measurements, accounting for particle interactions between acceleration and detection, and found that the turbulence-associated $\mathrm{sech}[(E/E_{\rm cut})^2]$ cutoff with a spectral index of $s \sim 2$–2.2 is supported by the data. This result contrasts with the significantly harder power-law indices needed by exponential cutoff models inspired by diffusive shock acceleration (Pierre Auger Collaboration 2017, 2023), which are incompatible with the expected $s \gtrsim 2$. Other acceleration mechanisms, such as magnetic reconnection, could potentially produce harder ion energy spectra with $s \sim 0$–2 (L. Comisso 2024) but only over a limited energy range $E \lesssim \sigma_{\delta B} m_i c^2$. For energies $E \gg \sigma_{\delta B} m_i c^2$, the asymptotic power-law index from magnetic reconnection returns to $s \sim 2$. Another potential way for producing a sharper-than-exponential cutoff involves energy losses in the accelerator, such as synchrotron losses, which would result in a cutoff of the form $\exp[-(E/E_{\rm cut})^2]$ (V. N. Zirakashvili & F. Aharonian 2007). However, the need for finely tuned energy losses and the absence of pileup in the observed spectrum of UHECRs (R. Protheroe 2004; V. N. Zirakashvili & F. Aharonian 2007) strongly disfavors this scenario.

Analytic analysis (R. J. Protheroe & T. Stanev 1999) suggests that the spectral cutoff in diffusive shock acceleration is exponential or softer, with spectral index $s \gtrsim 2$. If this behavior is borne out by the analysis of PIC simulations for shock acceleration, as we have done for magnetized turbulence, it will be possible to use the combined fit of UHECR spectrum and composition data to discriminate between acceleration mechanisms. While a comprehensive comparison of fits with different cutoffs is left for future work, within the framework of the analysis reported in Section 4, the exponential cutoff both gives a worse fit and requires a harder spectral index incompatible with theoretical expectation.

Highly magnetized turbulence, as considered in this study, is expected in a range of astrophysical environments, such as jets from AGNs (R. Blandford et al. 2019), outflows from neutron star mergers (K. Kiuchi et al. 2024), jets from collapsars (C. Thompson 1994), jetted tidal disruption events (B. Curd & R. Narayan 2019), and coronae of Seyfert galaxies (K. Murase et al. 2020). Determining which of these systems can meet the specific conditions required for the particle acceleration mechanism discussed here will be an essential next step in identifying the sources of UHECRs.

Acknowledgments

We thank Michael Unger and Teresa Bister for their feedback on the manuscript and Joseph Insley for his assistance with the visualizations. L.C. was supported by the National Science Foundation award PHY-2308944, G.R.F. by NSF PHY-2013199 and PHY-2413153, and M.S.M. by the NSF MPS-Ascend Postdoctoral Award #2138121. Computational resources were provided by the Innovative and Novel Computational Impact on Theory and Experiment (INCITE) program, using resources of the Argonne Leadership Computing Facility, which is a DOE Office of Science User Facility supported under Contract No. DE-AC02-06CH11357. Additional computational support was provided through Columbia University's Shared Research Computing Facility and NYU IT High Performance Computing resources, services, and staff expertise. We acknowledge the use of code created by Michael Unger under the EU-funded grant PIOF-GA-2013-624803 and further developed by Marco Muzio.

ORCID iDs

Luca Comisso https://orcid.org/0000-0001-8822-8031
Glennys R. Farrar https://orcid.org/0000-0003-2417-5975
Marco S. Muzio https://orcid.org/0000-0003-4615-5529

References

Abreu, P., Aglietta, M., Albury, J. M., et al. 2021, EPJC, 81, 966
Aloisio, R., Berezinsky, V., & Blasi, P. 2014, JCAP, 2014, 020
Alves Batista, R., Dundovic, A., Erdmann, M., et al. 2016, JCAP, 05, 038
Baker, S., & Cousins, R. D. 1984, NIMPA, 221, 437
Birdsall, C. K., & Langdon, B. 1985, Plasma Physics via Computer Simulation (New York: McGraw-Hill)
Blandford, R., & Eichler, D. 1987, PhR, 154, 1
Blandford, R., Meier, D., & Readhead, A. 2019, ARA&A, 57, 467
Blasi, P. 2013, A&ARv, 21, 70
Brunetti, G., & Lazarian, A. 2011, MNRAS, 410, 127
Buneman, O. 1993, Computer Space Plasma Physics, 67 (Tokyo: Terra Scientific)
Casse, F., Lemoine, M., & Pelletier, G. 2001, PhRvD, 65, 023002
Chen, C. H. K., Leung, L., Boldyrev, S., Maruca, B. A., & Bale, S. D. 2014, GeoRL, 41, 8081
Coleman, A., Eser, J., Mayotte, E., et al. 2023, APh, 147, 102794
Comisso, L. 2024, ApJ, 972, 9
Comisso, L., & Sironi, L. 2018, PhRvL, 121, 255101
Comisso, L., & Sironi, L. 2019, ApJ, 886, 122
Comisso, L., & Sironi, L. 2021, PhRvL, 127, 255102
Comisso, L., & Sironi, L. 2022, ApJL, 936, L27
Curd, B., & Narayan, R. 2019, MNRAS, 483, 565
Gilmore, R. C., Somerville, R. S., Primack, J. R., & Dominguez, A. 2012, MNRAS, 422, 3189
Goldreich, P., & Sridhar, S. 1995, ApJ, 438, 763
Greisen, K. 1966, PhRvL, 16, 748
Hillas, A. M. 2005, JPhG, 31, R95
Kempski, P., Fielding, D. B., Quataert, E., et al. 2023, MNRAS, 525, 4985
Kimura, S. S., Tomida, K., & Murase, K. 2019, MNRAS, 485, 163
Kiuchi, K., Reboul-Salze, A., Shibata, M., & Sekiguchi, Y. 2024, NatAs, 8, 298
Kundu, S., Singh, N. K., & Vaidya, B. 2023, MNRAS, 524, 4950
Lemoine, M. 2019, PhRvD, 99, 083006
Lemoine, M. 2023, JPlPh, 89, 175890501
Longair, M. S. 2011, High Energy Astrophysics (Cambridge: Cambridge Univ. Press)
Lynn, J. W., Quataert, E., Chandran, B. D. G., & Parrish, I. J. 2014, ApJ, 791, 71
Murase, K., Kimura, S. S., & Mészáros, P. 2020, PhRvL, 125, 011101
Muzio, M. S., & Farrar, G. R. 2023, ApJL, 942, L39
Muzio, M. S., Farrar, G. R., & Unger, M. 2022, PhRvD, 105, 023022
Pezzi, O., Blasi, P., & Matthaeus, W. H. 2022, ApJ, 928, 25
Pierre Auger Collaboration 2013, JCAP, 1302, 026
Pierre Auger Collaboration 2017, JCAP, 2017, 038
Pierre Auger Collaboration 2020a, PhRvL, 125, 121106
Pierre Auger Collaboration 2020b, PhRvD, 102, 062005
Pierre Auger Collaboration 2023, JCAP, 2023, 024
Pierre Auger Collaboration 2024a, arXiv:2406.06315
Pierre Auger Collaboration 2024b, JCAP, 07, 094
Pierre Auger Collaboration 2024c, arXiv:2406.06319
Pierre Auger Collaboration 2024d, PhRvD, 109, 102001
Protheroe, R. 2004, APh, 21, 415
Protheroe, R. J., & Stanev, T. 1999, APh, 10, 185
Riehn, F., Engel, R., Fedynitch, A., Gaisser, T. K., & Stanev, T. 2020, PhRvD, 102, 063002
Robertson, B. E., Ellis, R. S., Furlanetto, S. R., & Dunlop, J. S. 2015, ApJL, 802, L19
Schlickeiser, R., & Miller, J. A. 1998, ApJ, 492, 352

Spitkovsky, A. 2005, in AIP Conf. Ser., Vol. 801, Astrophysical Sources of High Energy Particles and Radiation, ed. T. Bulik, B. Rudak, & G. Madejski (San Francisco, CA: ASP), 345
Sun, X., & Bai, X.-N. 2021, MNRAS, 506, 1128
Telescope Array Collaboration 2023, APh, 151, 102864
Telescope Array Collaboration 2024, PhRvD, 110, 022006
Thompson, C. 1994, MNRAS, 270, 480
Thompson, C., & Blaes, O. 1998, PhRvD, 57, 3219
Unger, M., Farrar, G. R., & Anchordoqui, L. A. 2015, PhRvD, 92, 123001
Wong, K., Zhdankin, V., Uzdensky, D. A., Werner, G. R., & Begelman, M. C. 2020, ApJL, 893, L7
Yan, H., & Lazarian, A. 2002, PhRvL, 89, 281102
Zatsepin, G. T., & Kuz'min, V. A. 1966, JETPL, 4, 78
Zhdankin, V., Uzdensky, D. A., Werner, G. R., & Begelman, M. C. 2018, ApJL, 867, L18
Zirakashvili, V. N., & Aharonian, F. 2007, A&A, 465, 695